

Prediction of Periodic Centerline Porosity and Pulse Marks by CFD and Experimentation for Continuously Cast Copper



THOMAS D.A. JONES, RICHARD STRACHAN, KYLE RUSSELL,
MUSTAFE ABDULLAH, DAVID M. MACKIE, MERVYN COOPER, BRIAN FRAME,
and JAN B. VORSTIUS

For 8 mm OFCu rod, the formation of pulse mark defects on the exterior of the rod and periodic macroporosity (> 1 mm diameter pores) occurring internally along the centerline of the castings have been observed and noted to limit the maximum attainable withdrawal rates (~ 4 m/s). Conversely, the same casting defects have been witnessed for slower rates; therefore, investigations were performed to investigate how the casting motions (withdrawal, dwell, and pushback) formed these defects and could be prevented. Characterization of the physical properties of the cast rods by tensile testing and analysis by optical and computed tomography (CT) imaging revealed correlations to the outer pitch length marks on the rods and confirmed relationships to casting motions and pitch lengths evaluated from metallurgical equations. Computational fluid dynamic modeling using Ansys Fluent v.R1 was applied to quantify the localized formation and dissipation of periodic hotspots internally within the die for the different motions. A mechanism leading to periodic porosity was identified, which was irrespective of the average casting withdrawal rates and enabled prediction of the location, frequency, and magnitude of the macroporosity defect.

<https://doi.org/10.1007/s11663-022-02704-1>

© The Author(s) 2022

I. INTRODUCTION

THE production of large volumes of Cu alloys benefits from a vertical upward continuous casting (VUCC) process,^[1] specifically the casting of oxygen-free Cu metal (< 0.001 pct) (OFCu), which is used in applications related to conductive wiring, electric motor brazing, and particle accelerators, owing to the high use of oxygen-scavenging graphite materials applied within the crucible/dies.^[1] However, the VUCC process output is limited due to the occurrence of external and internal defects generated within the

casting setup, such that the casting motions applied display a maximum throughput after which successful casting is limited (4 m/s for OFCu 8 mm wire).^[1]

Considerable research has been made into the influence of continuous casting (CC) motions on the formation of casting defects.^[2–6] For CC, the typical motions comprise of a continuous withdrawal (out of the casting setup), a pause (dwell), or pushback (into the crucible/melt) coinciding with a remelt.^[3,7–9] CC may include a variety or combination of these motions, which are repetitive and can be referred to as a pulse sequence.^[1] External defects, such as *pulse marks*, appear as notches on the outer periphery of a directionally cast billet/wire and are witnessed in most CC alloy systems. They are formed as a result of the withdrawal motions and, if severe, can lead to cracking and unwanted particle entrapment.^[2] Within the author's previous work, pulse mark formation was noted on VUCC aluminum-bronze (Cu_{89wt pct}Al_{10wt pct}Fe_{1wt pct}), where the inclusion of pushback motion produced shallower marks,^[10] enabling reduced fracturing and higher tensile loads.

CC motions also influence internal defects produced within cast alloys such as pore cavities in the solidified cast piece, alternatively referred to as porosity or blowholes dependent on their appearance and formation mechanisms. The formation of macroscale (0.5 mm

THOMAS D.A. JONES, KYLE RUSSELL, MUSTAFE ABDULLAH, DAVID M. MACKIE, and JAN B. VORSTIUS are with the University of Dundee, School of Science and Engineering, Dundee, DD1 4NH, UK. Contact e-mail: t.d.a.jones@dundee.ac.uk RICHARD STRACHAN is with the University of Dundee, School of Science and Engineering and also with the Rautomead Ltd, Dundee, DD2 4UH, UK. MERVYN COOPER and BRIAN FRAME are with the Rautomead Ltd.

Manuscript submitted August 4, 2022; accepted December 1, 2022.
Article published online December 27, 2022.

scale) internal pore defects occurs for an increase of average CC velocity,^[11,12] which imparts a limiting value to the maximum velocities attainable from a casting rig and thus its throughput. Within CC Cu alloys, similar defects are also present limiting maximum velocities;^[13] however, for VUCC OFCu, porosity was also observed by the authors at lower speeds than the accepted maximum (4 m/s for 8 mm rod) and was attributed to the length of the casting motion (stroke length), where shorter casting motions led to smaller pore sizes and higher quality casting, independent of the average withdrawal velocity.

The porosity of OFCu additionally showed periodicity in its occurrence along the center longitudinal direction; however, periodic central porosity is sparsely reported in the literature. A study of CC steel billets^[14] highlighted a periodic appearance of internal centerline cavities and showed a small, weak correlation between pore periodicity and average casting speed; and other recent studies^[15] concluded further work was needed to identify the influence of average withdrawal velocity on centerline deformation formation, which this work shall address.

Centerline porosity occurring along the middle of the casting is associated with localized hotspot regions which are the last positions to solidify within a cast piece and lead to the formation of pores due to insufficient replenishment of fluid during solidification, the gasses within the spot, and thermal contraction of the outer encasing solid shell.^[16] The identification of hotspot regions can provide information on pore occurrence^[17,18] which typically occur in the center of short-freezing range alloys,^[19] such as OFCu. Physical *in situ* monitoring of thermal effects inside the die can be performed to identify hotspots by the drilling of thermal-couple sensors into the casting die to monitor temperature during CC,^[20] or by the use of computed tomography(CT) during CC to monitor the solidification front^[21–23]; however, both techniques are costly in their setup and may interfere with the casting process due to drilling into the die.

An alternative method is to apply computer modeling to predict the casting behavior and to identify hotspots, which can negate the need for a costly experimental setup.^[1] Computational fluid dynamic (CFD) modeling provides prediction of heat and solidification during casting.^[1] Recent CFD work by the authors^[1,24] highlighted the validation and verification of a finite-volume model developed in commercial software Ansys Fluent and indicated its use for predicting the influence of casting motions on 8 mm VUCC OFCu solidification.

Using this model on 8 mm diameter VUCC OFCu, investigations shall be made of (a) the influence of the different casting motions (withdrawal, pushback, dwell) on the occurrence and magnitude of periodic macroscale centerline porosity; (b) how the occurrence and magnitude of pulse mark defects produced on the outside of OFCu changes in response to motion; and (c) if the CFD model can provide original insight into the heat transport behavior which can be used to predict the maximal casting motions. Physical casting trials shall be performed to validate the simulated model, and

measurements of pulse marks and pores will be obtained from optical microscopy and CT scanning. The physical changes of the rod are characterized from tensile investigations.

The presented work highlighted the formation of periodic, interior macroscale pores of differing size, which were minimized by reducing the magnitude of the hotspots generated by applying a specific sequence of casting motions. The occurrence of exterior pulse marks defects was proportional to casting motions and their formation was predictable from metallurgical equations,^[4] as further verified in this work. The work details that from CFD modeling, further understanding was provided into the influence of casting motions on the generation of hotspot regions within the solidified region, whose appearance, frequency, and size correlated to physical measurements of centerline macroporosity and cast performance.

II. EXPERIMENTAL

A. Simulation Setup and Verification

Ansys Fluent v.R1 simulation was setup as outlined within Figure 1. In (a), a 2-D symmetrical approximation of the VUCC setup (highlighted in b), showing the die immersed to a standard depth within the OFCu melt, is shown. A symmetric design was chosen, modified from *simulation 2* within.^[1] For further details of setup including equations, mesh grid convergence verification, material values, boundary conditions, and transient time step settings, refer to online supplemental material section A.

B. Simulation Validation

The CFD model developed within Ansys Fluent was validated against thermal measurements obtained within the die in Reference 20 and highlighted a (± 10 pct) agreement with measured values, see supplemental section A4.

The simulation of VUCC solidification fronts using Ansys was validated for changes in casting motions (upwards, dwell and pushback), within^[1,25] by comparing simulated SF with the imprint made on the grain growth directions of the solidifying OFCu. The grain growth direction occurs tangential to the thermal isotherms (the SF) within a solidifying configuration^[26] and so, the simulated change in SF motions in response to casting motions was correlated to the notable imprints on the measured grain growth orientations of casting trials in,^[1] additionally, the heat values simulated by CFD were used as boundary conditions within the author's phase-field simulation work, which also confirmed predictions to grain growth directions.^[25] Together, these confirmed and validated the CFD technique for approximating the changes to SF shape for different speeds.

Lastly, values for the heat transfer coefficient were compared within this work with previous work by the authors^[1] and measurements, see Section III–D.

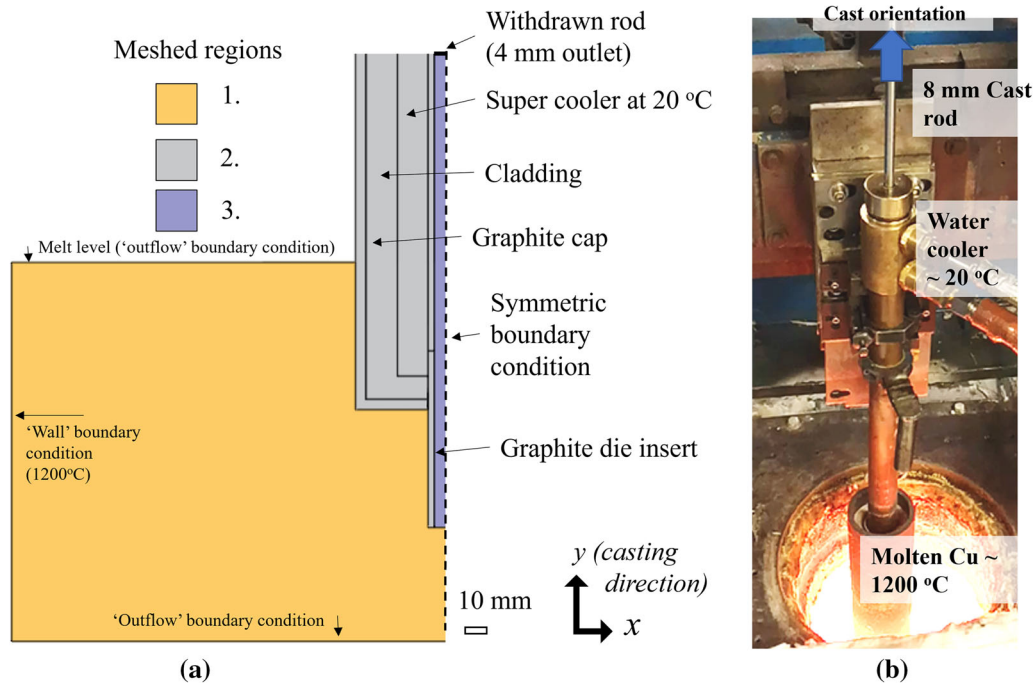


Fig. 1—(a) M2-D Simulation schematic of (b) casting setup.

C. Casting and Sample Analysis

Casting trials of settings outlined in Figure 2 were performed on 8 mm diameter OFCu in a VUCC machine by the authors at Rautomead Ltd (Figure 1b), and a length of rod was sampled for analysis. The motions chosen were selected to highlight different average cast velocities, different dwell periods, withdrawals, and pushback motions. Setting *c* was chosen as this approximated the maximal attainable casting rate with this configuration along with producing no casting defects. Settings *a*, *b* & *d* were also selected due to the centerline pores observed in their casting, prior to this work. Engineering stress strain analysis measurements of five samples of each setting were performed using an Instron 4202 tensile tester, which is a displacement-controlled operation of up to 50 kN load and with an inbuilt travel extensometer. The samples were intentionally not cast into a modified die to produce tensile test specimens to JIS 8B classification, but were instead cast in a standard circular 8 mm diameter die VUCC wire configuration, to best capture the typical occurrence of the casting defects produced. The samples were as-cast and were cut off into sections per sample cast, for test gauge lengths of 10 cm. The strain rate for the tests was a constant $5 \times 10^{-3} \text{ s}^{-1}$. The tensile fracture break modes were analyzed by sampling the section of the break using a MTI corporation STX-202A wire diamond saw and imaging under a (Spectrographic, NMM-800RF) optical microscope. For analysis of surface defects, optical images were obtained of the rod prior to tensile analysis and the image for setting *c* was enhanced using ImageJ software by applying a variance filter. For analysis of pores, a CT scanner (XTEK XT H 225ST) was used on a sample prior to

stress-strain analysis. For rod cross-sectional analysis under the microscope, sample preparation included grinding, polishing, and chemical etching was performed to conditions outlined within.^[27]

For simulation validation, the convection heat transfer coefficient (h_c) ($\text{W/m}^2\text{K}$) was evaluated from the center of the die to across the die wall (not to be confused with convective heat transfer coefficient which is evaluated over a smaller finite boundary) given by:

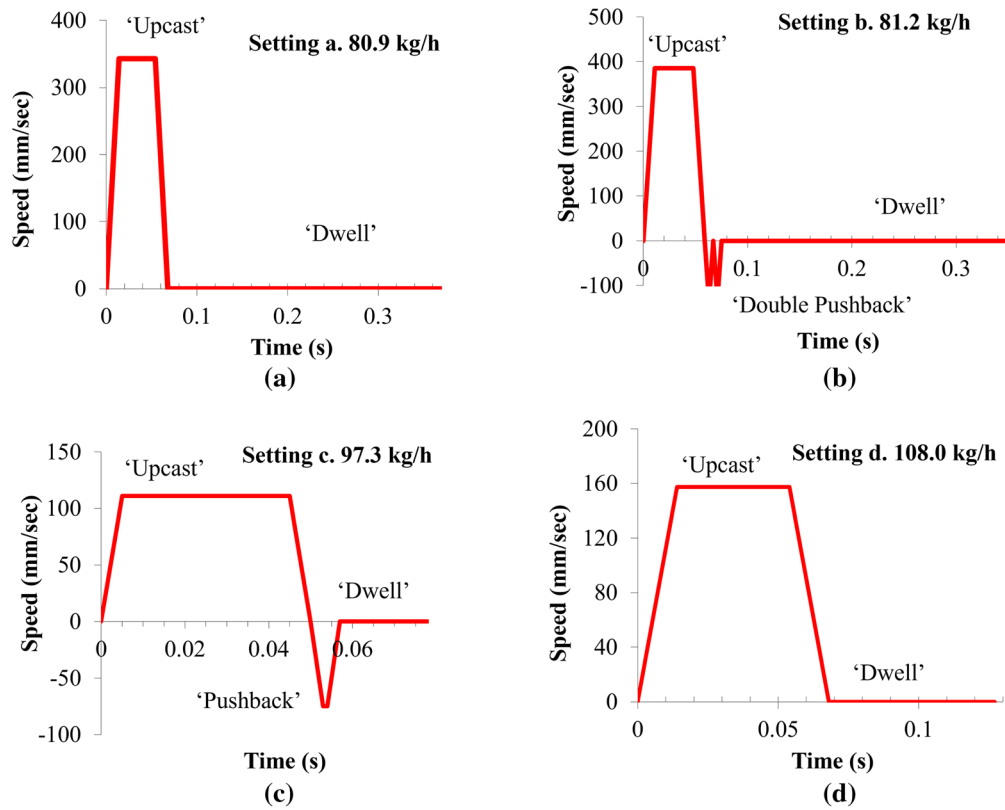
$$h_c = q_h / (T_s - T_{ref}) \quad [1]$$

where q_h is the heat flux, T_s is the temperature of the graphite die wall, and T_{ref} is the temperature of the liquid medium in the middle of the die.^[28] The values were then compared with literature values.

III. RESULTS AND ANALYSIS

A. Measured Physical Properties

The nominal stress-strain curves are highlighted in Figures 3(a), (b), for as-cast VUCC OFCu for two of the casting speed settings, *c* and *a*, which are settings showing no defects and with defects, respectively. For setting *c*, the curve displayed typical behavior for VUCC 8 mm OFCu, which was a ductile sample indicated by the reduction in stress prior to fracture point, and produced an average ultimate tensile strength (UTS) of $160 \pm 21 \text{ MPa}$ and fracture point of $33 \pm 3 \text{ pct}$, which were within the minimum industrial standard for electrical pure copper casting (155 MPa and 35 pct , for JIS H 5120 CAC102).^[29] The results also matched properties for upwards cast OFCu in.^[30]



Speed setting	Casting Rate (kg/h)	Average upwards velocity (m/s)	Total pulse duration (sec)	Upwards stroke (mm)	Dwell (sec)	×1 Pushback (sec)	×2 Pushback (sec)	Porosity present
a.	80.9	0.0501	0.369	18.5	0.301	N/A	N/A	Yes
b.	81.2	0.0503	0.348	18.5	0.273	0.11	0.11	Yes
c.	97.3	0.060	0.078	5.0	0.021	0.012	N/A	No
d.	108.0	0.067	0.127	8.5	0.059	N/A	N/A	Yes

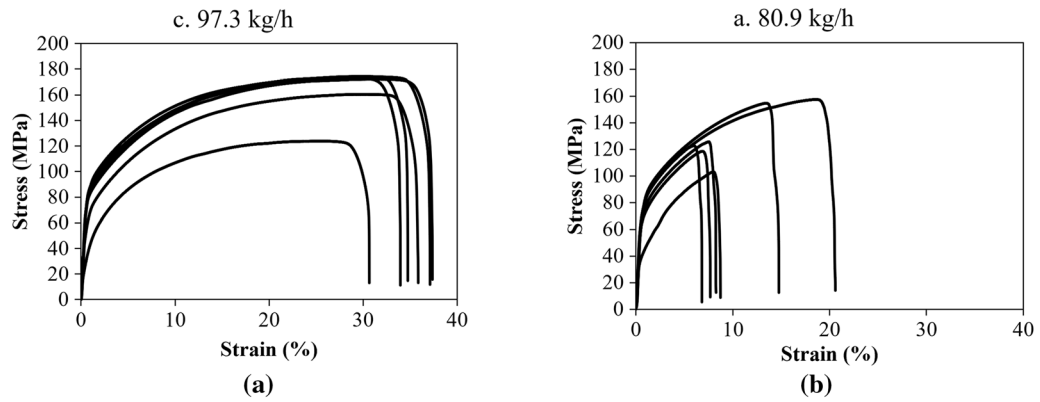
(e)

Fig. 2—(a) to (d), casting speed settings a to d, respectively. (e) Details of the casting motions.

Without the presence of defects, setting *c*, the UTS along with the fracture point increased. For all settings containing defects, the UTS and the fracture point were less, as highlighted in *c*). For all plots of stress–strain curves including samples *b* and *d*, see supplemental Figure S2.

To characterize the influence of defects on the tensile breaks, the fractographs (break sites) were investigated as highlighted in Figures 4(a) through (d), which showed optical images of the four different types of breaks witnessed across all samples and settings. These were divided as (a) *defect-free ductile breaks*, and (b) through (d) *defect-containing breaks*. In (a), a standard ductile break occurred characterized by necking and plastic deformation which was expected behavior for a defect-free Cu tensile test.^[30] This was witnessed solely within setting *c*, see *e*), which was as expected owing to the lack of witnessed defects in the cast rod, see Figure 2.

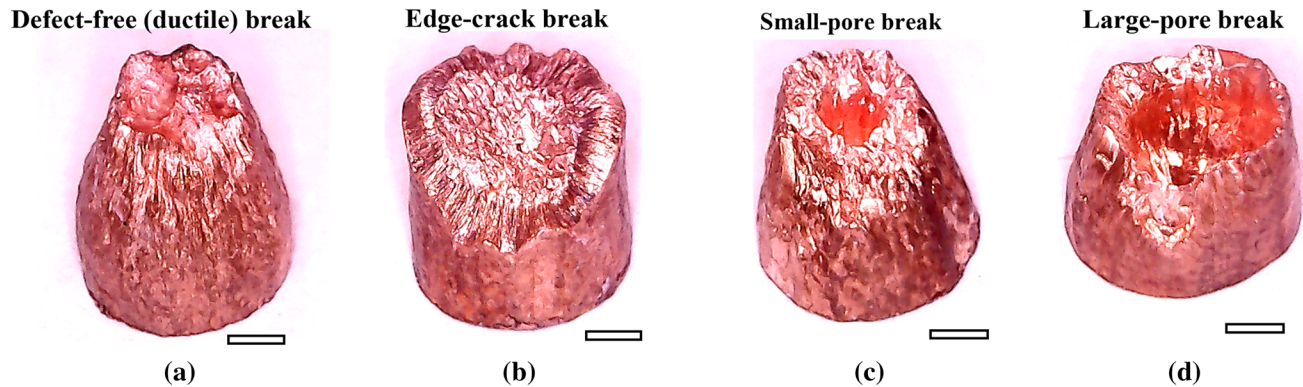
In (b), a brittle fracture mode was witnessed characterized by low necking or plastic deformation, and a rapid crack propagation at a normal to the axis of testing.^[31] This break was attributed to pulse mark-induced defects (see Figure 5), with the crack propagating initially along the outer edge of the rod along the grain boundaries and so was referred to here as an *edge-crack break*. This was highlighted by two grain patterns: columnar grains orientated centrally to rod axis and a central equiaxed (randomly orientated) region. The edge region corresponded to a fatigue pre-crack which is typically induced in tensile testing,^[32] however, it was caused here due to cracking formed during casting, see Section III–B, and the center region corresponded to mechanical fracture. This break type was witnessed within two settings (*a* and *b*) with more details of its occurrence discussed in Section III–B.



Setting & average speed	Average UTS (MPa)	Average Fracture Point (%)
a. 80.9 kg/h	130 ± 20	10 ± 5
b. 81.2 kg/h	109 ± 4	7 ± 1
c. 97.3 kg/h	163 ± 21	33 ± 2
d. 108.0 kg/h	138 ± 37	32 ± 7

(c)

Fig. 3—Nominal stress–strain data of OFCu cast samples. (a), (b) stress–strain curves and (c) tabulated results.



Percentage of numbers of break types

Setting & average speed	Defect-free (ductile) break (%)	Edge crack breaks (%)	Small-pore breaks (%)	Large-pore break (%)
a. 80.9 kg/h	0	63	13	25
b. 81.2 kg/h	0	60	40	0
c. 97.3 kg/h	100	0	0	0
d. 108.0 kg/h	33	0	33	33

(e)

Fig. 4—(a) to (d) optical images of tensile break locations, scale bars 2 mm. (e) summary of fractographs.

(c) and (d) highlighted macroscale pores which had occurred within the samples (discussed in greater detail in Section III-C) and were divided into small (diameters less than the radius of the rod, 4 mm) and large sizes (pores of diameters greater than the radius of the rods,

4 mm), respectively. These breakages showed some necking indicating plastic deformation prior to breakage, however, not to the same degree as the standard ductile break, (a). These pore breaks were witnessed in all samples other than setting *c*. The outer shells of the

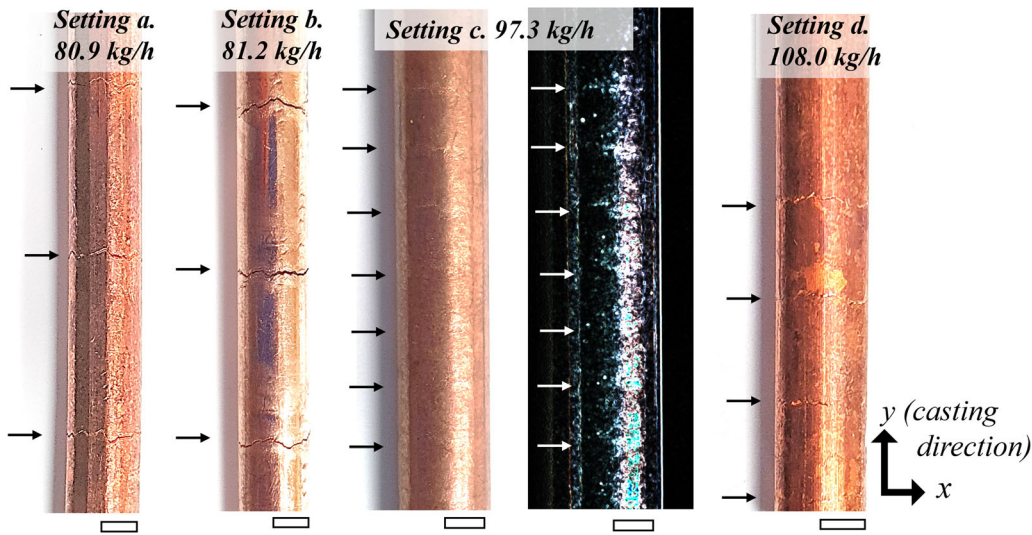


Fig. 5—Contrast enhanced, optical images of 8 mm diameter cast rods with 4 mm scale bars. Variance filtered image included alongside c.

rods after breaking were characterized by a texturing indicating large-grain deformation within the cast piece on tensile testing, which is typical for VUCC OFCu.^[30]

A summary of the breakages is given in (e) which showed that other than setting *c*, all settings were comprised of defect-induced breaks related to edge cracks and porosity.

B. Pulse Mark Defects in Response to Casting Motion

Optical images of the outside of the cast rods are shown in Figure 5 and they highlighted speed settings *a*, *b* & *d*. Crack defects in the samples ran tangential to the withdrawal direction along the outer edge and the distance between cracks differed as shown by the arrows. Setting *c* showed no cracks but pulse marks were apparent on its surface highlighted by arrows and an enhanced image (variance filtered) of setting *c* inserted for clarity.

The relationship for pulse mark separation distance (its pitch or pulse length, x) was confirmed from measurements in steel CC in^[4] as:

$$x = \frac{2\pi \cdot v_{cast}}{\omega} \quad [2]$$

where v_{cast} is the average velocity upwards (m/s) and ω is the angular frequency (rad/s) given by $2\pi/t$, where t is the total pulse duration. This simplifies to:

$$x = v_{cast}t \quad [3]$$

Using Eq. [2], the pitch was estimated, and the average pitch length was evaluated from measurements, see Figure 6(a). Figure 6(b) shows a plot of measured pitch against estimated values which showed a strong linear correlation (R^2 : 0.9994), for the different settings.

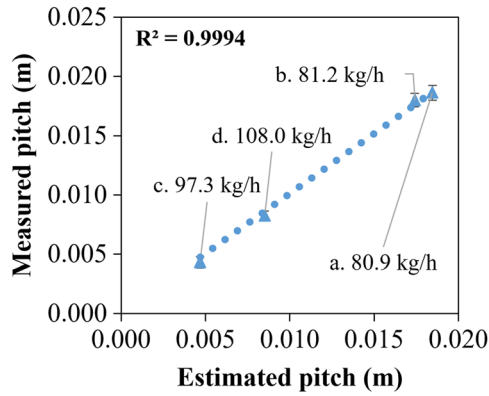
The measured pitch length was plotted against the upwards stroke length in (c) and also showed a linear relationship which highlighted shorter stroke lengths produced smaller pitch values; however, for the

inclusion of pushback motions, this behavior was not consistent, where setting *a* (80.9 kg/h, pulsed) showed a greater pitch than setting *b* (81.2 kg/h, double pushback), 19 ± 0.4 mm and 18 ± 0.6 mm, respectively. This was likely due to remelt occurring during the pushback motions, reducing the length of the pulse despite the same forward stroke motion applied for each setting (18.5 mm). This indicated that equation^[2] was a better approximation for pitch than stroke length as indicated in plot (b) and thus provided a greater insight into cast quality prior to casting.

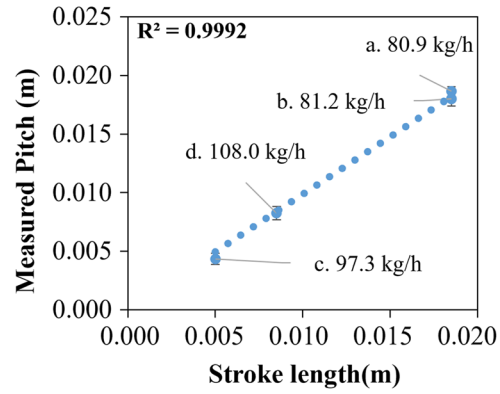
The pulse marks generated significant depressions for settings *a* and *b* and from these, the average depth and width of the depressions were evaluated from optical and CT measurements (see supplemental Figure S3 for cross-sectional images), and the results are summarized in d). Depressions could not be observed for settings *c*. The depressions in settings *a* and *b* displayed a shallow V-shape which is typically susceptible to cracking due to acting as stress risers.^[33] The depth of the edge depressions was measured for settings *a*, *b*, and *d*. When comparing the same stroke lengths, (18.5 mm, settings *a* and *b*), with the inclusion of pushback motions (setting *b*), the depression depth reduced considerably by ~ 80 pct (1.4 mm to 0.28 mm) possibly due to the remelting of the SF.^[33] This trend was also noted in CC steel literature^[34] and in the authors' previous CC copper work.^[10] The smallest depression depth, however, was observed for setting *d* at 0.04 ± 0.007 mm. This setting showed a smaller pitch length (0.008 ± 0.0006 m) than settings *a* or *b*, which indicated a proportional relationship between depression depth and pitch length, as also observed in steel CC literature.^[34–36] This relationship was attributed to an increase in the forces exerted and to the bending moment of the solidifying shell for longer stroke lengths resulting in greater pulse mark depths. A small reduction in the depression width was observed on the application of pushback motion and pitch length reduction.

Setting	Average upwards velocity (m/s)	Total pulse duration (sec)	Estimated pitch from equation 2 (m)	Average measured pitch ($\pm s.d$)(m)
a. 80.9 kg/h	0.0501	0.369	0.018	0.019 \pm 0.0004
b. 81.2 kg/h	0.0503	0.348	0.017	0.018 \pm 0.0006
c. 97.3 kg/h	0.060	0.078	0.005	0.004 \pm 0.0005
d. 108.0 kg/h	0.067	0.127	0.009	0.008 \pm 0.0006

(a)



(b)



(c)

Setting	Average pulse mark depth ($\pm s.d$) (mm)	Average pulse mark width ($\pm s.d$) (mm)
a. 80.9 kg/h	1.4 \pm 0.1	0.4 \pm 0.1
b. 81.2 kg/h	0.28 \pm 0.04	0.30 \pm 0.04
c. 97.3 kg/h	N/A	N/A
d. 108.0 kg/h	0.04 \pm 0.007	0.25 \pm 0.004

(d)

Fig. 6—(a) Measurements and estimation of pitch. (b) and (c) plots of measured pitch against estimated pitch and stroke length, respectively. (d) measurements of depression size.

The occurrence of the edge-crack breaks reported in Figure 4(e) was only noted for settings *a* and *b* which coincided with the observation of large pulse mark depressions (beyond 0.04 mm depth), further highlighting their correlation, and indicating that the depressions initiated breaking under tensile load.

The rod breakages highlighted in Figure 4(e) revealed the presence of defects within the rod. These defects were proportional to the pitch length where the shortest pitch coincided with defect-free casting, setting *c*. For pitch lengths between 4 and 19 mm (settings *c*, *d*, *a*, and *b*), the numbers of ductile defect-free breaks observed during tensile testing reduced to zero, which indicated that the mechanism for defect formation was influenced and increased for increasing pitch lengths. For setting *d*, the pitch length was 8 ± 0.6 mm and showed defects in the form of porosity (77 pct of breaks) and ductile breaks (33 pct); however, edge-crack breaks were lacking, as identified in Figure 4(b). This behavior indicated that for longer pitch lengths, defects occurred first in the form of porosity and then with edge-crack breakages. Further investigation of the influence of porosity was discussed in Section III-C.

C. Porosity Defects in Response to Casting Motion

The occurrence of porosity was measured from cross-sectioning of cast samples as highlighted by optical images of setting *a* in Figure 7. This setting showed the greatest occurrence of edge-crack breakages, of both small (pore diameters less than the radius of the rod, 4 mm) and large porosity (pores of diameters greater than the radius of the rods, 4 mm), see Figure 4. As highlighted in (a), pores of average size 0.067 ± 0.003 mm³ (measured by CT see Figure 9) were present occurring as *tear-shaped* pores, which were characterized by a larger *head* and short narrow *tail*. In this image, the tail was oriented vertically upward along the direction of withdrawal motion. Tear-shaped or ellipsoid pores can form due to strain deformations occurring after solidification of spherical pores, due to the forces transmitted to the solidifying material by the pinchers or rollers when withdrawing the metal piece, as noted in steel CC rolling literature.^[37] The magnitude and orientation of this deformation relates to the forces applied, so this effect could contribute to the tear-shaped features

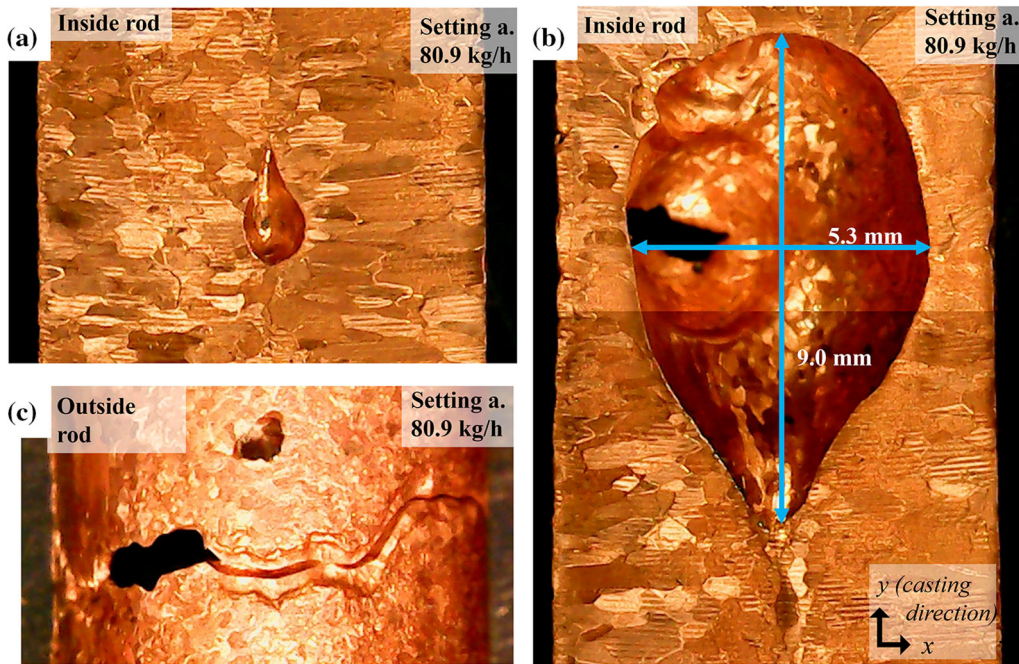


Fig. 7—Optical images of etched 8 mm diameter OFCu rod for setting a (80.9 kg/h). (a) Small pore inside rod vertical cross section. (b) Edge crack on outside of rod surface. (c) Large-pore cavity inside rod vertical cross section.

witnessed here; however, the distribution of heat within hotspots may also influence their orientation as discussed in Section III–D.

A region was highlighted in (b) and (c) showing the location of a large-scale pore of size approximately $170 \pm 1 \text{ mm}^3$ estimated from the optical image, from the inside and outside of the rod, respectively. Here, the large pore displayed a droplet appearance although with a tail pointing away from the cast direction. The outer edge revealed a hole on the side of the rod with a crack propagating horizontally across its cross section. The crack was likely an edge crack and the hole formed due to a rupturing of the thin shell of the solidifying rod as it was withdrawn from the casting rig. The three images highlighted the influence of the three noted defects influencing rod breakages: edge cracks, and small and large pores; however, the occurrence of the depressions here also coincided with the appearance of the large-pore cavity, which indicated that the mechanisms behind the two defects' formation were related.

The porosity formed within had spherical/ellipsoid structures with some uniformity and regular shape. This type of porosity is observed in pure metal casting such as OFCu and with Cu-Cr alloys due to volume shrinkage and insufficient liquid metal replenishment,^[29,38] with this affect discussed in more details in Section III–D. For a comparison with a defect-free rod, CT images of setting c are shown in supplemental Figure S5 and highlighted a dense uniform structure and a grain structure typical for OFCu: equiaxed smaller grains at the outer edge with larger columnar grains oriented toward the center axis.^[1]

Further analysis of the pore's position and form was obtained by CT scans of rods which had not been altered in any form after casting (stress tested or chemically etched), for all speed settings. The CT images for all settings were given within the supplemental, Figure S5 & S6. Optical and CT images of the two types of pores observed, large and small, are highlighted in Figure 8. Within a) are the images of setting d, which displayed a moderate occurrence of porosity and showed an optical image alongside a CT scan at equivalent location. A rupture was highlighted on the outer edge of the rod and inside, at the same location, by a large-pore cavity of size $26 \pm 1 \text{ mm}^3$ (estimated from CT image). The arrow annotation on the CT image highlighted where the rupture occurred and showed how the large pore's shape was oriented toward this location. The large-pore features showed similarity to surface blowhole defects, which are characterized by spherical porosity occurring close to the surface of a casting.^[39]

Highlighted in (b) was setting a, which yielded the most cast defects and showed the presence of small pores which occurred periodically and internally along the center axis of the rod. The pores were droplet-like in appearance and positioned center to the vertical axis, like the cross-sectional images within Figure 7. They showed similarity to centerline porosity induced due to shrinkage and a lack of liquid metal replenishment,^[39] however, additionally displayed periodicity. Their tails oriented in differing directions within the rod between casting pulses which highlighted a change in direction between casting cycles. The pulse mark depressions are shown within the image and highlighted its pitch length ($0.019 \pm 0.0004 \text{ m}$). To investigate the shape of the pores, further 3-D images of the pores from micro-CT

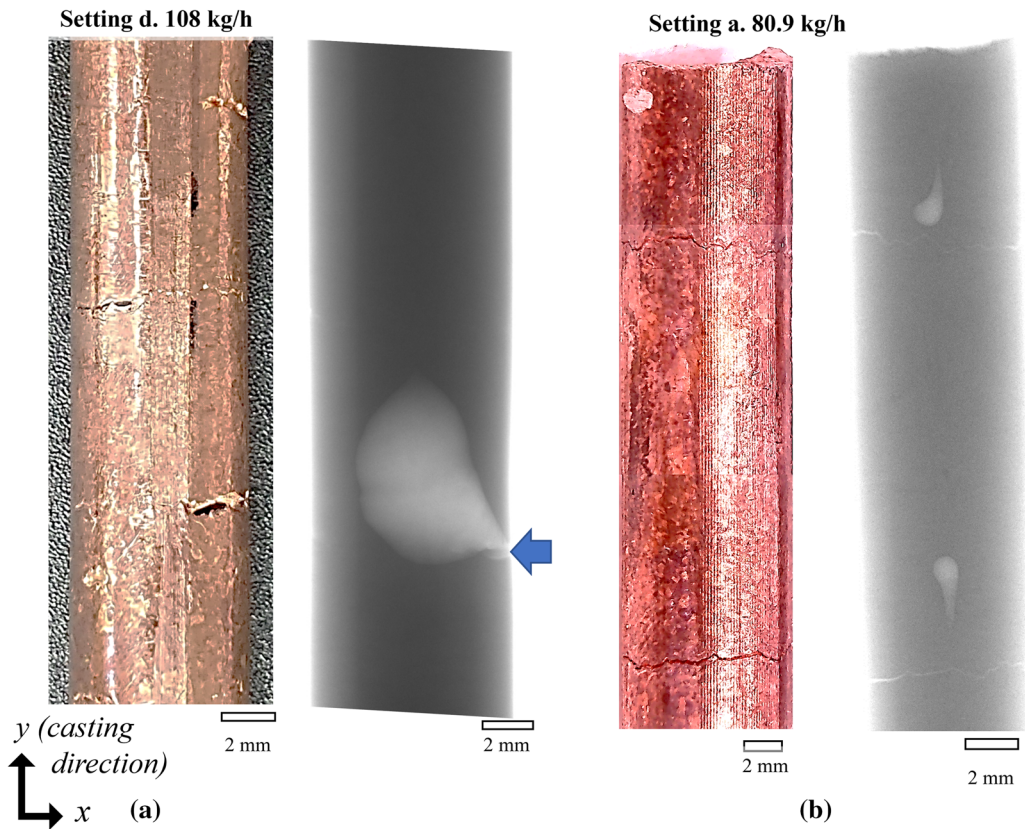


Fig. 8—Optical and CT images. (a) and (b) large- and small-pore features, respectively.

scans were obtained, see supplemental Figure S6. These CT results also indicated a change in orientation of the pore's tails along the axis of casting (y axis) as they were generated during the casting cycle. The tail orientation appeared to flip showing a moderate correlation to the casting period for the casting settings investigated. Simulations within Section III-D were performed to investigate this effect.

The small pore size (mm^3) and separation distance (m) were measured from the CT scans of small pores, see supplemental Figure S6, for the different settings (a , b & d , omitting c due to no macroporosity). The results are summarized in Figure 9(a). The small pore sizes were within the range of 0.067 to 1.4 mm^3 . In (b) and (c), the measured pitch lengths were compared with the small pore's separation distance in the y axis (casting orientation, see Figure 8) and pore volume, respectively. They showed strong and moderate positive correlations at R^2 0.9923 and 0.8971, accordingly, indicating that smaller pitch lengths resulted in smaller distances between pores and smaller volumes. In (d) and (e), the pitch was compared with the rod's physical properties of UTS and fracture length, which showed inverse moderate and strong correlations at R^2 0.7559 and 0.9465, respectively, indicating that smaller pitch lengths resulted in improved physical properties. The error bars were the standard deviation and so reflected the variance occurring between tested samples. The random presence of the large pores produced within the rods likely contributed to larger variances observed.

In summary, these important results highlighted that the mechanism for small-pore formation was linked to the casting motions occurring during the withdrawal of the rod and that the physical properties of the rod were related to the pitch length, where for this casting setup, pitch lengths around 4 mm (setting c) yielded no porosity or casting issues.

The occurrence of the small pores and large-pore cavities can be attributed to subsurface and surface blow holes, respectively, which are associated with a smooth interiors and pore diameters within the mm range, as highlighted in Figure 7.^[39,40] This cavity formation is associated with gas bubble formation which occurs when the local gas pressure exceeds the local metallostatic head of the liquid, leading to a bubble being blown into the liquid melt.^[39] A possible location for the gas bubble introduction within the casting die could be from the $100 \mu\text{m}$ air gap formed on solidification shrinkage of the rod,^[1] which resides between the thin solidified shell of the cast piece and the graphite die, see Figure 1. Porosity can also be due to gas entrainment from the melt caused by hydrogen combination with oxygen to form steam,^[41] however, all casting trials were performed on the same equipment which applied oxygen-scavenging graphite as the dies and crucible, thus minimizing the occurrence of porosity by steam. The introduction of air into the melt can also occur within the crucible, causing a systematic defect in the solidifying rod; however, all the casting trials were performed

Setting & average speed	Average small-pore volume (mm ³) ($\pm s.d.$)	Large-pore volume (mm ³)	Average distance between small-pores (mm) ($\pm s.d.$)
a. 80.9 kg/h	0.90 \pm 0.2	170 \pm 1	17 \pm 3
b. 81.2 kg/h	1.40 \pm 0.1	Not observed	14 \pm 6
c. 97.3 kg/h	Not observed	Not observed	N/A
d. 108.0 kg/h	0.067 \pm 0.003	26 \pm 1	8.0 \pm 1

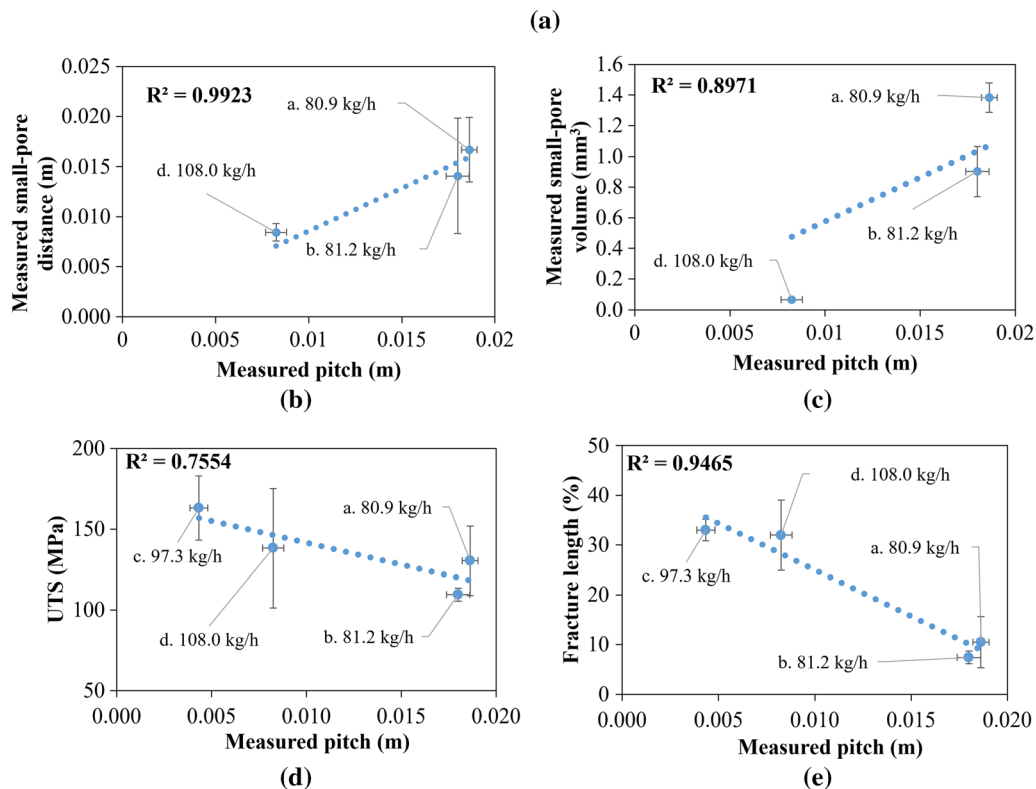


Fig. 9—(a) Summary of pore measurements. For different casting speeds, measured rod pitch length in response to measured small-pore (b) separation distance and (c) volume, and measured rod physical properties of (d) UTS and (e) fracture length.

sequentially on the same day and the porosity disappearance for setting *c* indicates that this systematic defect was not present.

The disappearance and change in appearance of the pores in response to the casting motions indicates that their formation was more likely influenced by solidification shrinkage mechanisms and physical deformations induced due to the casting motions rather than contamination effects.

D. Simulated Solidification Front

A simulation model was constructed built on previous work by the authors^[1] and verified in terms of mesh refinement and time step, and the outputs validated against measured die temperature values, see supplemental Figure S1. With this model, see Figure 1, simulations of the casting were performed of speed settings *a* through *d*, see Figure 2. The simulations were run until it reached equilibrium, defined here as a consistent output of liquid metal between the start and end of the casting cycle (the pulse duration defined within Figure 2).

The simulated SF for casting setting *a* (upward and dwell motions and showed the most defects) was highlighted within Figure 10 and showed from dark to light shades, liquid and solidified volume fractions of OFCu, respectively. As OFCu is a metal element rather than alloy, it displays a short-freezing range with little mushy zone; therefore, a discreet boundary forms between solid and liquid phases—its solidification front (SF). The region highlighted is a 2-D cross section of the 8 mm diameter Cu cast piece which is surrounded by a 2 mm thick graphite die walls, which do not have an allocated color in the diagram. SF was highlighted by a thin boundary between the liquid and solid phases of the OFCu (thickness added to SF postprocessing to highlight boundary), and timelapse images of the SF motions were shown within the 8 mm die at a location around the onset of solidification (at the supercooled within the casting setup, see Figure 1).

In a), a timelapse of the evolution of the SF over the duration 0 to 0.734 s was shown which was two casting pulse cycles of size 0.369 s. The SF was characterized by two features: localized isolated liquid droplets and a

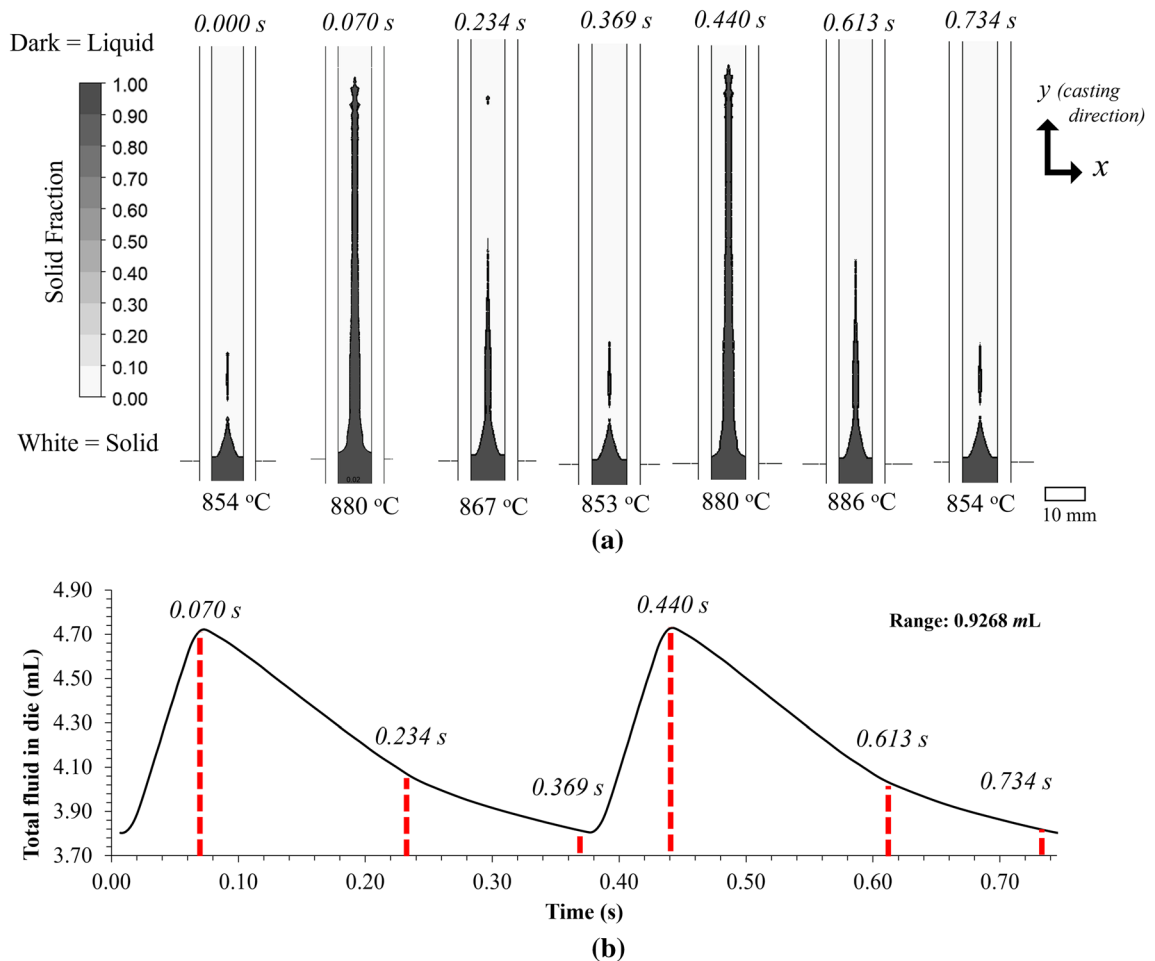


Fig. 10—(a) Time evolution of simulated solidification front for casting setting a, with inserts of the time period and average die temperature. (b) Plot of the simulated total fluid within the die over time.

large fluid cavity with a vertically upward orientation. The localized liquid droplets correlate to isolated hotspots which differed in position within the die, and appearance within the casting pulse cycle (the start and end, *etc.*). The SF appeared pointed upward owing to the direction of casting (upward) which is representative of VUCC OFCu.^[1] As the rod was withdrawn by upward motions, liquid Cu and heat were transported into the die from the crucible, as indicated by the dark shades and the 26 °C increase in average die temperature at 0.070 s. As the different casting motions were applied, the SF changed shape as well as height within the die. At the end of the upward motions, around 0.070 s and 0.440 s, the fluid volume within the die was at its greatest and its position the furthest up the die at 93 mm measured from the start of solidification at the edge of the die.

During the dwell cycle, starting after 0.070 s, the fluid volume decreased due to the transport of heat out of the die and the lack of further metal replenishment from the crucible. At this time around 0.234 s, the average die temperature reduced by 13 °C and the SF reduced in terms of length and breadth. At the end of the SF, a localized hotspot formed which broke away from the

main body of the retreating SF. This hotspot displayed a tear-shaped appearance with a tail pointed toward the retreating SF. Lower down within the die, a larger hotspot region was formed characterized by necking forming along the SF, which by 0.369 s broke away as the necking reduced in width, and formed its own tear-shaped hotspot. This hotspot was present at the start of the next casting cycle as shown at 0 s, 0.369 s, and 0.734 s. The orientation of this hotspot's tail was upward owing to the collapse of the neck of the retreating SF.

For this speed setting, isolated tear-shaped hotspots were generated with tails pointing in differing orientations, owing to the collapse of the necking regions within the SF at different times within the casting pulse and at different locations. To overcome the presence of the hotspots occurring at the beginning of the casting cycle, longer dwell times could be applied to allow for their dispersion by heat transport out of the die.

In (b), an output of the total liquid volume of OFCu within the 220 mm by 8 mm diameter die, which gave the total fluid volume measured within the die over the casting period and an indication of the rise in localized heat within the die, is shown. An increase in the volume

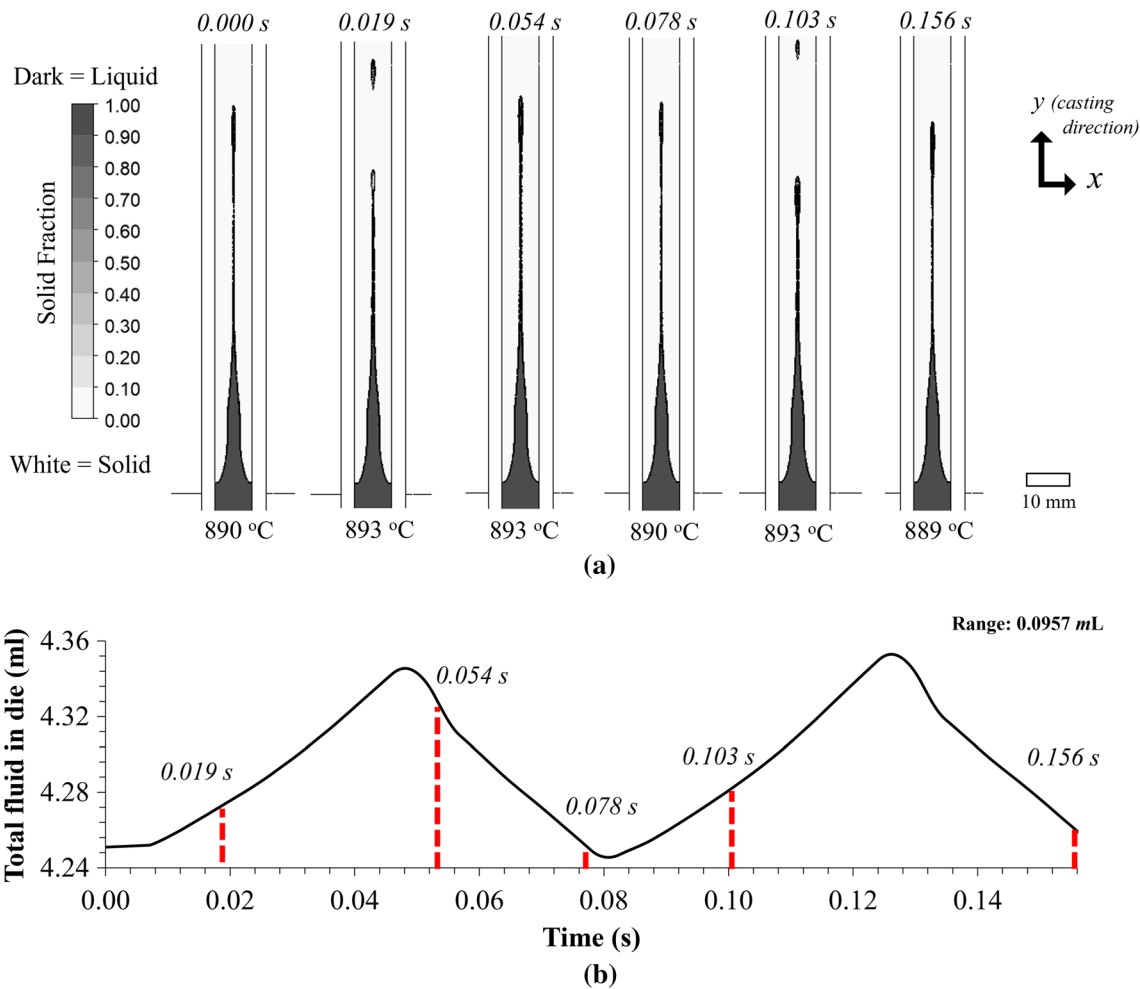


Fig. 11—(a) Simulation of SF within the casting die for setting *c* (upwards, dwell and pushback motions) for different times, with time step and average die temperatures annotated. (b) Plot of the change in total fluid volume within the die over two casting pulses.

of liquid metal which corresponded to the upward withdrawal motions was shown, followed by a reduction around 0.070 s due to the dwell motion. The cycle then repeated around 0.369 s for the next series of casting motions. The change in fluid over the period (the difference between the maximum and minimum fluid volume values—its range) was 0.9268 mL. This value indicated the total increase in the size of the liquid volume within the die during the casting pulse.

Highlighted within Figure 11 is the solidification mass fraction for setting *c* (containing upwards, pushback and dwell motions, and which produced no defects). Within (a) are timelapse images over the duration from 0 to 0.156 s, which was two casting pulse cycles of size 0.078 s, see Figure 1.

At 0 second, the SF shape showed a wide base followed by necking and lastly a larger spherical lobe. The upward motions caused the SF within the die to rise, and the magnitude of the upwards motions (110 mm/s) led to the spherical region breaking away from the SF as an isolated hotspot. This continued to rise in the die and to dissipate as it traveled upward. At the same time, the SF lower down continued to rise in

the die with a new spherical lobe forming at the end, as highlighted around 0.019 second. At this time, the isolated hotspot reached a maximum height of around 87 mm and was comparable to previously simulated lengths for that setting ($\sim 81 \text{ mm}^{[1]}$) with differences due to the increased accuracy of the current work due to the smaller time step sizes (courant number 0.7, see supplemental section A4). The isolated hotspot formed a tear shape with a tail pointing downward away from casting orientation and toward the SF. This was observed around the application of the withdrawal motion and was highlighted at 0.019 and 0.103 second, which were locations showing SF maximum heights within the die. Around 0.054 second, the subsequent application of pushback and dwell caused the SF to no longer rise within the die and to dissipate, as shown by a slight reduction in height and width up to the start of the next pulse cycle, around 0.078 second, where the behavior repeated.

The total liquid volume of OFCu was outputted as shown within (b). This indicated a rise in liquid metal corresponding to the upwards withdrawal motions followed by a reduction around 0.054 second due to

the dwell and pushback motions. The cycle then repeated around 0.078 second for the next series of casting motions. The total average fluid within the die was 4.3 ± 0.1 mL and the change in fluid over the period (its range) was 0.0957 mL. This change in fluid indicated an increase in size of the volume for the casting motions applied, which was approximately nine times smaller than for setting *a* (showing the most defects) and was caused due to the different casting motions applied. The simulated SF for settings *b* and *d* were highlighted within the supplemental in Figures S7 and S8, respectively, and showed similar behaviors in response to the casting motions. No notable trend was observed when comparing the simulated total average fluid volumes for the different settings; however, linear trends were observed for the change in fluid volume over the pulse cycle. These trends were discussed subsequently in Figure 12.

The simulated SF was influenced by a variety of factors which were controlled in the simulation by the software-specific parameters and the heat transport properties of the casting setting. The software-specific parameters include the approximation for the dampening coefficient $Amush$ occurring around the SF, the applied heat model (RANS $k-\omega$ SST), and the mesh and time step optimizations. These parameters were optimized within^[24] and mesh optimized within supplemental section A3, to give the closest approximation to the predicted SF behaviors for VUCC OFCu.

The casting settings influencing SF shape included the speed settings, the Marangoni flow which occurred at the liquid OFCu–graphite die interface, and the airgap approximation occurring after solidification due to shrinkage between the OFCu and graphite die. The Marangoni flow and the air gap approximation applied in this work were optimized in^[1,24] and kept constant.

Highlighted within Figure 12(a) is a summary of the outputted simulated values of the change in fluid volume and the average convection heat transfer coefficient (h_c) measured from the die for the different speed settings. The values showed no linear correlation with the average casting speeds highlighting an independence from the average upward casting motions. The h_c was output for each setting for simulation validation and produced values between 4.28×10^4 W/m²K and 9.02×10^4 W/m²K for the different speeds, which were comparable to previously simulated values by the authors 9×10^4 W/m²K^[1] and other OFCu simulated literature values $(0.955\text{--}1.896) \times 10^3$ W/m²K^[42] and measured values for water-cooled copper $(0.13$ to $1.2) \times 10^4$ W/m²K.^[43] There was no discernible trend of the average h_c in response to the casting speeds investigated.

The change in volume was compared with the casting defect features: measured pitch lengths and measured small-pore volumes, in (b) and (c), respectively. These plots showed strong linear positive correlations with R^2 values 0.9758 and 0.9465, respectively, indicating that for the generation of smaller liquid volumes during casting, small pitch lengths (associated with higher quality casting see Section III–B) and smaller pores were generated.

The simulated change in fluid volume provided an approximation to the liquid volume and the isolated hotspot volumes generated temporarily within the die for each setting, as the rise in liquid metal was associated with raises in temperature as highlighted within Figures 10 and 11. The correlation between liquid hotspots and pore formation has been commonly reported,^[17,18,23] noting again shrinkage and a lack of fluid feeding as the formation of porosity around the isolated hotspot. The initiation of the pore growth is typically reported to occur in regions where liquid flow is resisted and/or isolated, which differs in form dependent on the casting configurations and the speed settings applied in its withdrawal. The tear drop-shaped hotspots observed within this work represented locations where liquid flow was hindered. The initiation of porosity there could occur first around the tail region of the hotspot, as at the tail regions, these were the first to dissipate and solidify as shown in the simulation (see Figure 11). As such, the overall shape of the porosity could also mimic the shape of the hotspots or contribute to an asymmetry of the pore as witnessed within the CT images shown in Figure 8.

The simulated fluid volume was larger than the measured small-pore sizes. This was in line with other modeling research,^[17] where simulated hotspot was approximately five times greater than the total porosity produced in response to the solidifying spot; however, these values were produced due to alterations to simulation parameters to match CT image data, rather than being driven from first principals, and their setup was for a long-freezing range alloy rather than the short-freezing range metal within the current work, which has a different porosity formation mechanism owing to mushy zone movement.

The formation of the large pores were not witnessed periodically and for all casting speeds, however, the change in fluid volume simulated did correlate to the size of the large pore, where for settings *d* and *a*, large-pore volumes of 26 ± 1 mm³ and 170 ± 1 mm³ were witnessed for simulated liquid volumes of 249.0 mm³ and 926.8 mm³, respectively.

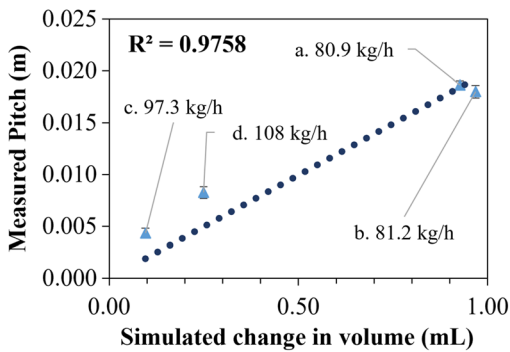
The simulated change in fluid volume was compared with the physical properties of the rod, its UTS, and the fracture length in Figures 12(d) and (e), respectively. The UTS and fracture lengths showed a moderate and strong inverse correlation at R^2 : 0.7582, and R^2 : 0.9854, respectively. Both showed inverse linear relationships indicating that for the generation of larger volumes of liquid within the die (greater than 0.0957 mL), the rod's strength and fracture length decreased owing to the formation of porosity and edge cracks.

E. Discussion on Casting Speeds Settings

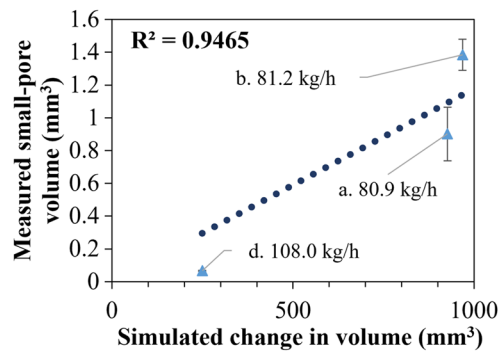
The three different casting motions, withdrawal, pushback, and dwell, applied within this work and their influence on VUCC OFCu are summarized in Table I along with findings from other CC literature. Significant studies report on the formation of pulse marks on the cast piece due to intermittent motions applied when casting and note relationships between the depths of

Setting & average speed	Simulate change in fluid (mL)	h_c (W/m ² K)
a. 80.9 kg/h	0.9268	6.27×10^4
b. 81.2 kg/h	0.9683	6.04×10^4
c. 97.3 kg/h	0.0957	4.28×10^4
d. 108.0 kg/h	0.2490	9.02×10^4
[1]	n/a	9.00×10^4
[42]	n/a	$(0.955 - 1.896) \times 10^3$
[43]	n/a	$(0.13 - 1.2) \times 10^4$

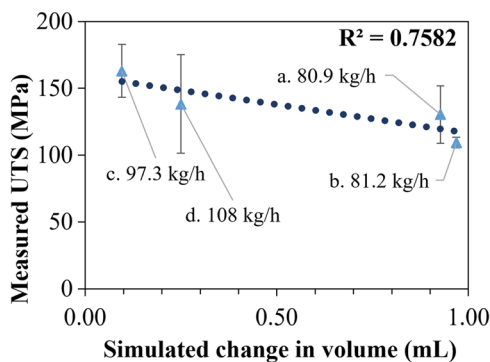
(a)



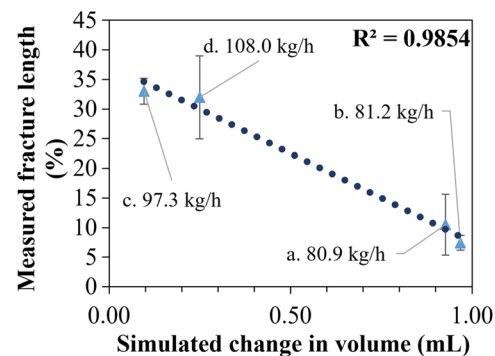
(b)



(c)



(d)



(e)

Fig. 12—(a) summary of simulated properties. Comparison of simulated change in fluid volume against measured (b) pitch length, (c) small-pore volume, (d) UTS and (e) fracture length.

these pulses and the formation of crack defects. Changes to the casting motions by reductions to the withdrawal length (stroke) are reported to reduce these features^[2,34–36] as also witnessed in the current study. When selecting a stroke length, minimizing this value along with the total pulse duration led to defect-free casting (setting *c*) which was summarized by one value given as the pitch length (Eq. [2]). This contributed toward improved physical properties which are essential for the subsequent rolling or drawing operations performed after casting.

To achieve more rapid speeds and higher throughputs, it is noted that the application of dwell and pushback motions are required, as they contribute to increased solidified shell strengths^[8,44] and a reduction in unwanted sticking of the cast piece to the inner die

walls.^[44,45] The current work highlighted the formation of internal microporosity defects for slower speeds (where slower speeds are typically associated with better casting quality^[11,12]), despite the additional inclusions of dwell and pushback motions. A relationship to the formation of hotspots and porosity was noted, which were generated within the die due to the complex interplay of the casting motions.

When choosing the motions to maximize the average throughput of OFCu, a trade-off occurred between the magnitude of the withdrawal and dwell motions. When the withdrawal motions were increased, it additionally increased the speed; however, at the expense of greater die-heat, whereas increased dwell times allowed for greater heat dissipation but at the expense of average casting speeds. The pushback motions additionally

Table I. Summary of Casting Motions

Casting Motion	Observed Effect
Withdrawal (Upwards)	generates pulse marks when combined with intermittent motions which are minimized by reduction to withdrawal (stroke) length ^[2,34–36]
Dwell (Motion Pause)	increases temperature and liquid volume within die ^[1,20] (Figs. 10 & 11) causes pulse marks on outer die edge due to change in solidification conditions ^[2] reduces sticking of cast piece to die ^[44,45] causes relaxation of casting motions (Figs. 10 & 11) enables heat transported out of the die and reduction to the liquid volume within die (Fig. 10) reduces size of hotspots (Fig. 10)
Pushback (Downwards)	reduces friction and sticking in some casting configurations ^[3] maintains a more consistent solidified shell ^[8,44] increases heat transported out of the die (Fig. 11) reduces size of hotspots (Fig. 11) causes reduction to pulse mark length and depth (Figs. 5 & 6)

helped to counter this effect by rapidly reducing the formation of heat within the die, allowing for shorter dwell durations and more rapid withdrawal motions (setting *c*). The inclusion of pushback also simultaneously reduced the occurrence of exterior casting defects by minimizing the pitch lengths for that setting.

The optimal combination of motions reduced the external and internal defects, while enabling access to more rapid casting throughputs.

IV. CONCLUSION

OFCu rods were VUCC cast at different speeds which comprised of different combinations of casting motions, withdrawal, dwell, and pushback. It was noted that two common defects occurred in the rod independent of the average withdrawal rate, porosity, and pulse marks. The physical properties of the rods were measured from stress–strain tests and the occurrence of four different fracture types was identified whose origins were attributed to standard, defect-free ductile breaks; edge-crack breaks influenced by the exterior pulse mark defects; and small and large-pore breaks, influenced by porosity. The exterior pulse marks were identified and their negative influence on casting was minimized by reducing the stroke length and the casting pulse duration, which were summarized by the single output in the pitch length equation. With this, casting defects were minimized for shorter pitch lengths and their occurrence could be estimated for this configuration prior to casting.

The internal macroporosity was evaluated from CT and optical images and highlighted small periodic centerline porosity, and large pores which did not show periodicity and were oriented toward ruptures on the surface. The small pores were tear-shaped in appearance and were associated with the formation of the small-pore breaks and the large pore with the large-pore breakages. A linear correlation was identified between

the physical size of the pores and the cast pitch length and an inverse correlation with the cast physical properties (UTS and fracture length).

Further analysis of the defects were made by modeling the heat transported within the die from 2-D, CFD simulations for the different speeds. The simulations revealed a periodic variation to the liquid metal present within the die, whose magnitude and shape correlated to the casting motions. Isolated hotspot features which showed a tear-shaped appearance were present and indicated a potential relationship between the hotspot shape and subsequent pore shape. Heat generated within the die was reduced by combinations of the different casting motions, which correlated with smaller pore sizes in the final cast piece and fewer to no casting defects.

The results highlighted that cast configuration could be optimized by applying CFD modeling and using equations to predict and minimize the pitch length, which lead to reduced numbers of cast trials and saved material use and costs.

ACKNOWLEDGMENTS

The authors thank Innovate UK for their financial support under Grant Project Number 117521.

CONFLICT OF INTEREST

On behalf of all authors, the corresponding author states that there is no conflict of interest.

OPEN ACCESS

This article is licensed under a Creative Commons Attribution 4.0 International License, which permits use, sharing, adaptation, distribution and reproduction

in any medium or format, as long as you give appropriate credit to the original author(s) and the source, provide a link to the Creative Commons licence, and indicate if changes were made. The images or other third party material in this article are included in the article's Creative Commons licence, unless indicated otherwise in a credit line to the material. If material is not included in the article's Creative Commons licence and your intended use is not permitted by statutory regulation or exceeds the permitted use, you will need to obtain permission directly from the copyright holder. To view a copy of this licence, visit <http://creativecommons.org/licenses/by/4.0/>.

SUPPLEMENTARY INFORMATION

The online version contains supplementary material available at <https://doi.org/10.1007/s11663-022-02704-1>.

REFERENCES

1. T.D.A. Jones, R.I. Strachan, D.M. Mackie, M. Cooper, B. Frame, and J.B. Vorstius: *Eng. Sci. Technol. an Int. J.*, 2021, vol. 24, pp. 92–104.
2. J.K. Brimacombe, S. Kumar, C.O. Hlady, and I.V. Samarasekera: in *INFACON 6*, SAIMM, Cape Town, 1992, pp. 7–23.
3. M. Ishikawa, A. Honda, and T. Anzai: *Trans. Iron Steel Inst. Japan*, 1980, vol. 20, pp. 570–77.
4. M. Vynnycky, S. Saleem, K.M. Devine, B.J. Florio, S.L. Mitchell, and S.B.G. O'Brien: *R. Soc. Open Sci.*, 2017, vol. 4, p. 170062.
5. M. Vynnycky and M. Zambrano: *Appl. Math. Model.*, 2018, vol. 63, pp. 243–65.
6. K.M. Devine, M. Vynnycky, S.L. Mitchell, and S.B.G. O'Brien: *IMA J. Appl. Math.*, 2020, vol. 85, pp. 385–420.
7. US3817313A: 1972.
8. S.A. Tavolzhanskii and I.N. Pashkov: *Metallurgist*, 2021, vol. 64, pp. 1068–76.
9. E.-R. Bagherian, Y. Fan, M. Cooper, B. Frame, and A. Abdolvand: *Met. Res. Technol.*, 2016, vol. 113, p. 308.
10. E.-R. Bagherian, Y. Fan, M. Cooper, B. Frame, and A. Abdolvand: *Metall. Res. Technol.*, 2016, vol. 113, p. 502.
11. J. Svizelova, M. Tkadleckova, K. Michalek, M. Strouhalova, and T. Ltd: in *METAL 2017: 26TH INTERNATIONAL CONFERENCE ON METALLURGY AND MATERIALS*, 2017, pp. 235–40.
12. H.S. Whitesell and R.A. Overfelt: *Mater. Sci. Eng. A*, 2001, vol. 318, pp. 264–76.
13. F.A. Fasoyinu, M. Sadayappan, D. Cousineau, M. Sahoo, AFS, and AFS: in *TRANSACTIONS OF THE AMERICAN FOUNDRYMEN'S SOCIETY, VOL 106*, vol. 106, 1998, pp. 721–34.
14. K.-H. Tacke: *Metall. Mater. Trans. B*, 1999, vol. 30B, pp. 751–61.
15. D. Jiang, W. Wang, S. Luo, C. Ji, and M. Zhu: *Int. J. Heat Mass Transf.*, 2018, vol. 122, pp. 315–23.
16. I.H. Katzarov and J.R. Popov: *Int. J. Heat Mass Transf.*, 1996, vol. 39, pp. 2861–67.
17. W. Li and J. Cui: *Int. J. Cast Met. Res.*, 2003, vol. 15, pp. 319–23.
18. V. Khalajzadeh and C. Beckermann: *Metall. Mater. Trans. A*, 2020, vol. 51A, pp. 2239–54.
19. A. Reis, Y. Houbaert, Z. Xu, R. Van Tol, A.D. Santos, J.F. Duarte, and A.B. Magalhães: *J. Mater. Process. Technol.*, 2008, vol. 202, pp. 428–34.
20. K. Härkki and J. Miettinen: *Metall. Mater. Trans. B*, 1999, vol. 30B, pp. 75–98.
21. M.M. Hytros, J.-H. Chun, R.C. Lanza, and N. Saka: *J. Manuf. Sci. Eng.*, 1998, vol. 120, pp. 515–22.
22. D. Tourret, J.C.E. Mertens, E. Lieberman, S.D. Imhoff, J.W. Gibbs, K. Henderson, K. Fezzaa, A.L. Deriy, T. Sun, R.A. Lebensohn, B.M. Patterson, and A.J. Clarke: *Metall. Mater. Trans. A*, 2017, vol. 48A, pp. 5529–46.
23. V. Khalajzadeh, D.D. Goettsch, and C. Beckermann: *Metall. Mater. Trans. A*, 2019, vol. 50A, pp. 757–1.
24. T. Jones, J. Vorstius, D. Mackie, R. Strachan, M. Cooper, and B. Frame: *Mater. Sci. Forum*, 2021, vol. 1106, pp. 642–47.
25. R. Strachan, T. Jones, D. Mackie, M. Cooper, B. Frame, and J. Vorstius: in *10th European Conference on Continuous Casting*, 2021.
26. D.A. Porter and K.E. Easterling: *Phase Transformations in Metals and Alloys*, 3 (Revised Reprint) Taylor & Francis, Boca Raton, 1992.
27. ASTM International, *ASTM E112-13, Standard Test Methods for Determining Average Grain Size*, 2013.
28. A. Neale, D. Derome, B. Blocken, and J. Carmeliet: in *Proceedings of the 11th NBEC Canadian Building Science and Technology Conference*, NBEC, 2007.
29. I. Goto, S. Aso, K. Ohguchi, K. Kurosawa, H. Suzuki, H. Hayashi, and J. Shionoya: *Mater. Trans.*, 2019, vol. 60, pp. 2–9.
30. T. Knych, B. Smyrak, and M. Walkowicz: *Prz. Elektrotechniczny*, 2011, vol. 87, pp. 285–90.
31. J.R. Davis: *Tensile Testing*, 2nd ed. ASM International, Washington, DC, 2004.
32. D.N. Londe, T.J. DR, and D.R. RAO: *Int. J. Eng. Sci. Technol.*, 2010, vol. 2, pp. 4130–36.
33. G. Lojen, A. Stambolić, B. Šetina Batič, and R. Rudolf: *Metals*, 2020, <https://doi.org/10.3390/met10040505>.
34. P. Lundkvist and B. Bergquist: *Ironmak. Steelmak.*, 2014, vol. 41, pp. 304–09.
35. J. Sengupta, B.G. Thomas, H.-J. Shin, G.-G. Lee, and S.-H. Kim: *Metall. Mater. Trans. A*, 2006, vol. 37A, pp. 1597–611.
36. K. Schwerdtfeger and H. Sha: *Metall. Mater. Trans. B*, 2000, vol. 31B, pp. 813–26.
37. X. Zhao, J. Zhang, S. Lei, and Y. Wang: *Steel Res. Int.*, 2014, vol. 85, pp. 1533–43.
38. BDG: *BDG Reference Sheet, P211, Volume Deficits of Castings Made from Copper and Copper Alloys*, 2010.
39. R. Monroe: *ChemInform.*, 2006, <https://doi.org/10.1002/chin.200642218>.
40. M. Latte and P. Chougule: *Int. J. Eng. Res. Technol.*, 2011, vol. 10(1), pp. 626–31.
41. J.R. Davis, ASMIIH Committee: *Copper and Copper Alloys*, ASM International, Washington, DC, 2001.
42. M. Uoti, M. Immonen, and K. Härkki: *Continuous Casting 2000*, pp. 143–48.
43. M. Bamberger and B. Prinz: *Mater. Sci. Technol.*, 1986, vol. 2, pp. 410–15.
44. T. Nozaki and S. Itoyama: *Trans. Iron Steel Inst. Japan*, 1987, vol. 27, pp. 321–31.
45. K. Nakai, Y. Umeda, Y. Sugitani, and M. Miura: *Trans. Iron Steel Inst. Japan*, 1984, vol. 24, pp. 983–91.

Publisher's Note Springer Nature remains neutral with regard to jurisdictional claims in published maps and institutional affiliations.